



|                  |                                                                                                                                                                                  |
|------------------|----------------------------------------------------------------------------------------------------------------------------------------------------------------------------------|
| Title            | Thermal structure beneath Far Eastern Russia inferred from geothermobarometric analyses of mantle xenoliths: Direct evidence for high geothermal gradient in backarc lithosphere |
| Author(s)        | Yamamoto, Junji; Nishimura, Koshi; Ishibashi, Hidemi; Kagi, Hiroyuki; Arai, Shoji; Prikhod'ko, Vladimir S.                                                                       |
| Citation         | Tectonophysics, 554-557, 74-82<br><a href="https://doi.org/10.1016/j.tecto.2012.06.005">https://doi.org/10.1016/j.tecto.2012.06.005</a>                                          |
| Issue Date       | 2012-07-25                                                                                                                                                                       |
| Doc URL          | <a href="http://hdl.handle.net/2115/50083">http://hdl.handle.net/2115/50083</a>                                                                                                  |
| Type             | article (author version)                                                                                                                                                         |
| File Information | Tec554-557_74-82.pdf                                                                                                                                                             |



[Instructions for use](#)

Thermal structure beneath Far Eastern Russia inferred from geothermobarometric analyses of mantle xenoliths: direct evidence for high geothermal gradient in backarc lithosphere

Junji Yamamoto<sup>\*,a,b</sup>, Koshi Nishimura<sup>c,d</sup>, Hidemi Ishibashi<sup>e,f</sup>, Hiroyuki Kagi<sup>e</sup>, Shoji Arai<sup>g</sup>, Vladimir S. Prikhod'ko<sup>h</sup>

<sup>a</sup> The Hokkaido University Museum, Nishi 8, Kita 10, Kita-ku, Sapporo 060-0810, Japan

<sup>b</sup> Institute for Geothermal Sciences, Kyoto University, Noguchibaru, Beppu 874-0903, Japan

<sup>c</sup> Natural Science Laboratory, Toyo University, 5-28-20 Hakusan, Bunkyo-ku, Tokyo 112-8606, Japan

<sup>d</sup> Institute for Geo-Resources and Environment, AIST, Tsukuba Central #7, Tsukuba 305-8567, Japan

<sup>e</sup> Geochemical Research Center, The University of Tokyo, 7-3-1 Hongo, Bunkyo-ku, Tokyo 113-0033, Japan

<sup>f</sup> Earthquake Research Institute, The University of Tokyo, 1-1-1 Yayoi, Bunkyo-ku, Tokyo 113-0032, Japan

<sup>g</sup> Department of Earth Sciences, Faculty of Science, Kanazawa University, Kakuma, Kanazawa 920-1192, Japan

<sup>h</sup> Institute of Tectonics and Geophysics (Far Eastern Branch, Russian Academy of Sciences), 65 Kim Yu Chen Str., Khabarovsk 680063, Russian Federation

\*Corresponding author: Junji Yamamoto

(Tel.: +81-11-706-4733; e-mail: jyama@museum.hokudai.ac.jp)

## 1. Introduction

Surface heat flow is a useful characteristic that indicates the thermal structure of the upper mantle. In general, the surface heat flow reflects tectonic activity and tectonic age in a region (e.g., Artemieva, 2006; Pollack et al., 1993;). For example, Archean cratons are characterized by low surface heat flow of  $42 \pm 10 \text{ mW/m}^2$  (Currie and Hyndman 2006 and references therein). In contrast, high heat flow of greater than  $100 \text{ mW/m}^2$  is observed in subduction zones (Yamano, 1995; Yamano and Uyeda, 1988). The question arises: how much heat flow does the intermediate zone, i.e. the backarc, have? The presence of active volcanism is well-known as a prominent feature of the backarc region. Although the origin of backarc volcanism has persisted as an insoluble problem, it can be linked with the subduction system. If longstanding arc-like volcanism exists in a region, then high heat flow can be expected.

Cascadia is a backarc where detailed scrutiny of surface heat flow has been undertaken (e.g., Blackwell et al., 1990a, 1990b). For Cascade, high surface heat flow ( $75 \pm 15 \text{ mW/m}^2$ ) is distributed across the backarc region (Hyndman and Lewis, 1999; Currie

et al., 2004; Currie and Hyndman, 2006; Hyndman et al., 2005). Some studies have been conducted to explain the high surface heat flow by mantle convection in the backarc asthenosphere (Currie et al., 2004; Currie et al., 2008; Currie and Hyndman, 2006; Kukačka and Matyska, 2008). Currie et al. (2008) present a numerical model showing that shearing of the backarc lithosphere by subduction-induced mantle flow can trigger gravitational instability of the mantle wedge, resulting in high surface heat flow and lithospheric thinning. However, an anomalous weak lithosphere rheology or an initial thermal structure that is significantly hotter than the average Phanerozoic continental geotherm is necessary to produce lithospheric thinning (Currie and Hyndman, 2006; Currie et al., 2008). Kukačka and Matyska (2008) describe a modeled mantle wedge flow driven by subducting plates. Strong pressure-dependence of viscosity or weak lithosphere rheology is necessary to reproduce the high surface heat flow in a backarc region. Such rheological data are not well examined.

Another backarc region whose thermal structure of the upper mantle has been investigated intensely is that of the marginal basins in the western Pacific, where hundreds of Cenozoic basalt fields cover an area of 3000 km. Many reports have

described that the shallower part of the upper mantle throughout the backarc region in eastern Asia shows characteristic low P-wave velocity with  $> 2\%$  compared to Archean craton (Duan et al., 2009; Huang and Zhao, 2009; Huang et al., 2010; Sadeghi et al., 2000; Tian et al., 2009; Zhao et al., 2009, 2010). Such seismic observations are not consistent with the mantle convection model proposed to explain the high surface heat flow in Cascade because vigorous mantle convection in the backarc mantle eliminates the local distribution of low seismic wave velocity anomaly. Elucidation of the origin of the local seismic anomaly in eastern Asia offers a clue to clarification of the mantle dynamics in the backarc.

The first question to be discussed is whether the low seismic velocity corresponds to high mantle temperature or not. For example, a seismic P-wave anomaly of a few percent is explainable by other conditions: the mantle is rich in water or pyroxenes. Direct measurements of temperature in the Earth's crust are limited to around ten kilometers in depth. Therefore, pressure and temperature (P–T) information of mantle-derived xenoliths in the backarc deserves attention. Temperatures at greater depths in the backarc could be ascertained if we were able to obtain the P–T information of the mantle xenoliths

accurately. Several reports have described the P–T information of mantle xenoliths sampled at backarc regions (Cascade: Ross, 1983; Saruwatari et al., 2001, South America: Lucassen et al., 1999, Aleutians: Akinin et al., 1997, Sea of Japan: Yamamoto et al., 2007, Far Eastern Russia: Yamamoto and Kagi, 2008; Yamamoto et al., 2002). The P–T information from Cascade and the Aleutians presents considerable uncertainty because garnet is absent from the mantle xenoliths. Generally, garnet is absolutely necessary to estimate the pressure information of mantle xenoliths using the pressure dependence of the pyrope breakdown reaction into orthopyroxene solid solution. For South America, reliable P–T information was reported based on thermobarometric analyses of mafic granulite xenoliths including garnet (Lucassen et al., 1999). It remains unclear, however, whether the P–T information of the xenoliths is representative of thermal structure of the current backarc because the xenoliths erupted in the Mesozoic Era (75–130 Ma).

An alternative geobarometry that is applicable to garnet-free xenoliths has been proposed: fluid-inclusion geobarometry (e.g., Miller and Richter, 1982; Roedder, 1983).

When the host magma traps and entrains a mantle xenolith to the Earth's surface, a CO<sub>2</sub>

inclusion in the mantle xenolith can retain CO<sub>2</sub> fluid density as high as that at the time of trapping. The pressure at which the mantle xenolith was trapped can be estimated from the intersection of the equilibrium temperature with an isochor in the phase diagram of CO<sub>2</sub>. If the pressure values obtained from some mantle xenoliths in a sampling site have a positive correlation with the equilibrium temperature, then the most likely explanation for the correlation is that they reflect the geotherm or heat flow of the sampling site. The geobarometry applies residual pressure of fluid inclusion as a depth probe. For the Sea of Japan, extremely high heat flow of 130–150 mW/m<sup>2</sup> was estimated using the method (Yamamoto et al., 2007). The Sea of Japan was formed in a short period by magma eruption between the Eurasian continent and the Japan arc at 11–17 Ma (Kaneoka et al., 1990). The plate models, GDH-1 (Stein and Stein, 1992) and CHABLIS (Doin and Fleitout, 1996), representing the thermal evolution of the cooling oceanic lithosphere, respectively show that the surface heat flow of the oceanic lithosphere with age of 11–17 Ma is 120–150 mW/m<sup>2</sup>, which is analogous to the xenolith geotherm, which is good evidence that fluid inclusion geobarometry can provide P–T information reflecting backarc geodynamics.

For Far Eastern Russia (Fig. 1), the P–T information of two mantle xenoliths (En-1 and En-010), which erupted at 4–5 Ma in Far Eastern Russia, has been reported (Yamamoto and Kagi, 2008; Yamamoto et al., 2002). Reports of these studies did not discuss the thermal structure because the mantle xenoliths show practically identical P–T values. Additional data might open the way to estimation of geothermal gradient in this region. This report presents discussion of the cause of the anomaly in seismic wave velocity in eastern Asia based on additional P–T information of mantle xenoliths from Far Eastern Russia.

## 2. Geological background

Northwestern Pacific marginal regions have played a part in subduction zones as active continental margins or volcanic arcs since the Mesozoic era. Cenozoic volcanic provinces are distributed over their backarc regions, which are called "hot regions" (Miyashiro, 1986). Volcanic and plutonic rocks that erupted in the late Cretaceous to the Pliocene in

Far Eastern Russia, where it comprises Precambrian continental basement (Ishiwatari and Tsujimori, 2003). Mesozoic magmatism in Far Eastern Russia is associated with subduction of the Izanagi Plate (Zonenshain et al., 1990). Subsequent tholeiitic basaltic volcanisms during the Eocene to Early Mid-Miocene occurred in the eastern part of Far Eastern Russia. The chemical compositions of the basalts suggest that they were derived from depleted residual asthenospheric mantle and that they are closely related to subduction because they show depletion in high-field strength elements (HFSE) and similar Sr–Nd isotopic compositions to that of MORB (Okamura et al., 2005). On reaching the age of the Sea of Japan opening (11–17 Ma), volcanism in this region altered its chemical compositions. Magmatisms after the Sea of Japan opening include alkaline and sub-alkaline basalts with wide ranges in trace element abundances. The trace element pattern, which resembles that of ocean island basalt, shows no clear depletion in HFSE (Okamura et al., 2005). Results of previous studies suggest that the changes in chemical compositions of the basalts are attributable to the transition from arc to intra-plate magmatism associated with backarc rifting (Esin et al., 1995; Okamura et al., 1998; Tatsumi et al., 2000).

### 3. Samples

Alkali basalts that erupted after the Sea of Japan opening include abundant mantle xenoliths. We sampled the mantle xenoliths from Ennokentiev, Sikhote-Alin, Far Eastern Russia (Fig. 1), and selected six xenoliths, which were all spinel-lherzolites and which were sufficiently large to support several analyses. The eruption age of host basalt for the xenoliths is 4–5 Ma (Sato, 1999). The younger eruption age carries the advantage that we can compare the petrological geotherm estimated from P–T information of the mantle xenoliths with the present-day geophysical investigation of large-scale thermal structure of the lithospheric mantle.

The mantle xenoliths have allotriomorphic granular and protogranular textures. These show no association with the surrounding host basalt, except for marginal grains of the xenoliths. The average grain sizes of their constituent minerals are ca. 1.0–2.5 mm. In this study, we estimate the depth provenance of the mantle xenoliths using residual

pressure of fluid inclusions. Almost all minerals have fluid inclusions with a negative crystal shape, except sample En-41 (Fig. 2). According to results of micro-Raman spectroscopic analyses, the fluid inclusions comprise pure CO<sub>2</sub> (> 99%): Raman spectra show no trace of components other than CO<sub>2</sub>, although a tiny quantity of Raman-inactive noble gases was extracted from the inclusions (Yamamoto et al., 2004).

To obtain precise depth information from residual pressure in a fluid inclusion, it is important to select a fluid inclusion with several aspects considered, i.e., diffusive loss of fluid from a fluid inclusion, fracture or decrepitation for fluid inclusion leakage, a maturity of a fluid inclusion. Yamamoto et al. (2011) evaluated the retentivity of CO<sub>2</sub> in fluid inclusions in mantle xenoliths including a sample En010, and discussed ideal conditions of a fluid inclusion to obtain the depth provenance of mantle xenoliths. For this study, we selected fluid inclusions adapting to the conditions.

#### 4. Major element compositions of mantle xenoliths

Major element analyses of mantle xenoliths were performed using an electron probe

microanalyser (JXA8800; JEOL) with WDS at the Earthquake Research Institute of The University of Tokyo. Analyses were conducted with an accelerating voltage of 15 kV, a beam current of 10 nA, and spot size of ca. 10  $\mu\text{m}$  diameter. Five points in each grain and five grains in each xenolith were analyzed. Table 1 shows the average compositions of 25 measurements for each mineral species. Correction procedures followed the method of Bence and Albee (1968). Integrated times for measurements were 100 s for most elements and 20 s for Na and K. The equilibrium temperature was estimated using a two-pyroxene geothermometer of Wells (1977). The equilibrium temperature typically has precision of  $\pm 20^\circ\text{C}$  (e.g., Ackerman et al., 2007). Clinopyroxenes in En2A have somewhat variable major element compositions. For example, the clinopyroxenes show two peaks in CaO contents of 19.7 wt% and 21.5 wt%, which corresponds respectively to equilibrium temperatures of  $959^\circ\text{C}$  and  $1040^\circ\text{C}$ . Therefore, it is necessary to infer uncertainty of around  $\pm 50^\circ\text{C}$  for the equilibrium temperature of En2A. The variation in CaO content of clinopyroxenes in En2A might reflect imperfect reequilibration caused by local thermal perturbation.

Major element compositions of the samples are presented in Table 1. The Fo value

( $[\text{Mg}/(\text{Mg} + \text{Fe}) \times 100]$  of olivine) and Cr# ( $[\text{Cr}/(\text{Cr} + \text{Al}) \times 100]$  of spinel) in the present samples respectively show values of 88–92 and 9–13. Those values are typical of upper-mantle lherzolite (e.g. Arai, 1994), indicating that the samples were derived from the fertile subcontinental lithospheric mantle. The range in equilibrium temperature was as wide as 912–1022°C, which contrasts with some previous reports (912°C for En-1 (Yamamoto et al., 2002) and 931°C for En-010 (Yamamoto and Kagi, 2008)). Both the wider range of equilibrium temperatures and accumulation of data enable us to estimate the proper geothermal gradient in this region.

##### 5. CO<sub>2</sub> fluid density and depth provenance of mantle xenoliths

The fluid (CO<sub>2</sub>) densities in CO<sub>2</sub> inclusions were determined using densimetry for CO<sub>2</sub> with micro-Raman spectroscopy (Kawakami et al., 2003; Yamamoto and Kagi, 2006; Yamamoto et al., 2002). We followed the analytical procedures for density measurements performed by Yamamoto and Kagi (2008).

Table 2 shows the results of micro-Raman spectroscopic analyses. No fluid inclusion with negative crystal shape exists in sample En-41. Therefore, densities of CO<sub>2</sub> in CO<sub>2</sub> inclusions were obtained from five mantle xenoliths. The Delta value, which is split between two main peaks of Raman spectra of CO<sub>2</sub>, can be converted to CO<sub>2</sub> density using a relation between CO<sub>2</sub> density and Delta value proposed by Yamamoto and Kagi (2006) (Table 3). Variation exists in CO<sub>2</sub> density among host mineral species; the density decreases in the order of spinel > orthopyroxene – clinopyroxene >> olivine. The CO<sub>2</sub> densities specific to mineral species in mantle xenoliths have been reported frequently (Sapienza et al., 2005; Schwab and Freisleben, 1988; Yamamoto and Kagi, 2008; Yamamoto et al., 2002, 2007). The low CO<sub>2</sub> density in olivine is attributed to the volume expansion of CO<sub>2</sub> inclusions resulting from plastic deformation of the surrounding crystal lattice in response to differential pressure between internal and outside pressure of fluid inclusion during the ascent of mantle xenoliths (Andersen and Neumann, 2001; Yamamoto et al., 2002, 2007, 2008). Actually, Yamamoto et al. (2011) reported that the orthopyroxene showed a sparse distribution of dislocations around a CO<sub>2</sub> inclusion, whereas olivine showed dense dislocations around CO<sub>2</sub> inclusions, implying that the low

CO<sub>2</sub> density of the CO<sub>2</sub> inclusions in olivine results from volume expansion of the CO<sub>2</sub> inclusions through plastic deformation of the host mineral during annealing of the xenoliths in ascending magma. However, the effect of the volume expansion for pyroxenes and spinel is negligible because of their high resistance against plastic deformation (Yamamoto et al., 2008).

The variation in CO<sub>2</sub> density between pyroxenes and spinel reflects elastic properties of the minerals (Yamamoto and Kagi, 2008). Zhang (1998) proposed an equation for the volume variation ( $\Delta V$ ) of a spherical inclusion in an anisotropic mineral based on the bulk modulus ( $K$ ), elastic constants ( $C_{ij}$ ), and thermal expansivity ( $\alpha$ ). The equation proposed by Zhang (1998) is

$$\frac{\Delta V}{V_0} = \frac{P_0}{K} + \alpha \cdot \Delta T + \frac{3}{(1-x)y} \times \left[ \frac{P_{inxy} - P_{out}}{(n-0.5)C_{33} + 2C_{13}} + \frac{P_{iny} - P_{out}}{(n+0.5)C_{33} - 2C_{13}} \right], \text{ (Eq. 1)}$$

where  $V_0$ ,  $P_0$ ,  $P_{in}$ ,  $P_{out}$ ,  $\Delta T$ , and  $n$  respectively represent the initial inclusion volume, the pressure where the xenolith was trapped by host magma, the present internal pressure of the inclusion, the pressure on outer surface of host mineral, and the temperature change,  $n$

$= 0.5 [1 + 8 (C_{11} + C_{12} - C_{13}) / C_{33}]^{1/2}$ . Actually,  $x = (R_i/R_h)^{2n}$  and  $y = (R_i/R_h)^{1.5-n}$ , where  $R_i$  and  $R_h$  respectively denote the inclusion radius and the host mineral radius. They are assumed respectively for this study as 10  $\mu\text{m}$  and 1 mm. In the estimate,  $P_{in}$  was converted from the observed  $\text{CO}_2$  density.  $P_0$  was calculated from the observed  $\text{CO}_2$  densities and the equilibrium temperatures were estimated using a two-pyroxene geothermometer. Strictly speaking, it is inappropriate to apply the observed  $\text{CO}_2$  densities for the calculation of the volume variation of  $\text{CO}_2$  inclusions ( $\Delta V$ ) because these values are uncorrected for the elastic change in volume of  $\text{CO}_2$  inclusions that occurred during transport of the mantle xenoliths. The elastic change is, however, negligible for the estimate of  $\Delta V$  because variation in the observed  $\text{CO}_2$  density of ca. 1% corresponds to that in the volume variation rate ( $\Delta V/V_0$ ) of only 0.02%. Elastic constants and thermal expansivity of mantle minerals were reported from some studies such as those by Weidner et al. (1978) and Saxena et al. (1993).

By applying the equation (Eq. 1), we estimated the volume variation rate ( $\Delta V/V_0$ ).

The densities of  $\text{CO}_2$  in  $\text{CO}_2$  inclusions were obtained from orthopyroxenes in all the mantle xenoliths except for En-41. Consequently, the corrected  $\text{CO}_2$  density in

orthopyroxene was adopted as representative of that in each mantle xenolith. Table 4 presents the calculated volume variation rate and the corrected CO<sub>2</sub> densities for orthopyroxenes.

Here we estimate the depth provenance of the mantle xenoliths based on the corrected CO<sub>2</sub> densities and the equilibrium temperatures. The depth (pressure) where the mantle xenoliths had been equilibrated with surrounding condition in the lithospheric mantle can be estimated from the intersection of the equilibrium temperature with isochors in the phase diagram of CO<sub>2</sub> (Fig. 3). The obtained pressures were 0.89–1.12 GPa. Assuming that the lithosphere density in Far Eastern Russia is 2.85 g/cm<sup>3</sup>, then the depth provenance of the mantle xenoliths is 32–40 km. Geophysical data indicate crustal thickness of 25–30 km in this region (Karp and Lelikov, 1990). Therefore, the mantle xenoliths were derived from the uppermost mantle beneath Far Eastern Russia.

## 6. Discussion

## 6.1. Heat flow in Far Eastern Russia

Before turning to a discussion about heat flow in Far Eastern Russia, we should clarify the influence of host magma on the equilibrium temperatures recorded in the mantle xenoliths. The possibility exists that the major element composition of constituent minerals in a mantle xenolith is reequilibrated during entrainment by host magma. Here we briefly calculate the time scale necessary for the reequilibration of the equilibrium temperature. The equilibrium temperatures of the mantle xenoliths were estimated using a two-pyroxene geothermometer. Partition of Ca between orthopyroxene and clinopyroxene is the most important part of the estimation. The most recent study (Zhang et al., 2010) reports a diffusion coefficient of  $^{44}\text{Ca}$  in diopside as  $3.2 \times 10^{-21} \text{ m}^2/\text{s}$  at  $1000^\circ\text{C}$  along the c-axis of diopside, which is the crystal axis of diopside with the fastest diffusion rate, which indicates that the Ca ion takes 2.5 million years to migrate  $500 \mu\text{m}$  within a diopside at  $1000^\circ\text{C}$ , even along the fastest diffusion axis. Mantle xenoliths are entrained to the Earth's surface in several days (Milashev, 1988). Consequently, even with consideration of the subsequent cooling period, the equilibrium temperatures

recorded in mantle xenoliths reflect the mantle temperature.

Spinel lherzolite exists at depths of 30–60 km (1–2 GPa) where good geobarometers based on mineral chemistry are not available. Geobarometry using residual pressure of the fluid inclusion is the only way to investigate the depth provenance of spinel peridotite xenoliths. The P–T values of the present mantle xenoliths line up from the lower left to the upper right in Fig. 3. The most likely explanation for the trend is that they reflect the geotherm beneath Far Eastern Russia. According to theoretical terrestrial heat flow presented in Fig. 3, the trend corresponds to the heat flow that is equal to or greater than  $100 \text{ mW/m}^2$ . Such heat flow is higher than that of Archean cratons ( $42 \pm 10 \text{ mW/m}^2$ ; Currie and Hyndman, 2006). The heat flow lies in the range of the volcanic arc ( $100\text{--}200 \text{ mW/m}^2$ ; Yamano, 1995; Yamano and Uyeda, 1988). Subsection 6.2 presents discussion of whether the high heat flow is consistent with the P-wave velocity structure of this area.

## 6.2. P-wave velocity structure of Far Eastern Russia

The seismic P-wave tomography in eastern Asia has been described in many reports (e.g., Duan et al., 2009; Huang and Zhao, 2009; Huang et al., 2010; Ichiki et al., 2006; Tian et al., 2009; Zhao and Ohtani, 2011; Zhao et al., 2009, 2010). The tomographic images clearly specify the occurrence of a stagnant slab in eastern Asia. Another distinctive feature of the tomographies is that low P-wave velocity anomaly is commonly observed in backarc regions. Furthermore, a prominent low P-wave velocity anomaly with  $> 2\%$  compared to ambient mantle is clearly imaged in the shallower mantle beneath Far Eastern Russia (Zhao et al., 2010). In the upper mantle, the P-wave velocity is affected by several factors such as temperature, petrological composition, and water content. For example, the P-wave velocity has positive correlation with Fo# and has negative correlation with the temperature and water content. Regarding Fo#, for pressures of less than 20 GPa, the P-wave velocity decreases by 2.0% (Speziale et al., 2005) or 2.2% (Núñez-Valdez et al., 2010) with decreasing Fo# from 90 to 81. The low P-wave velocity is not, however, ascribed to the lower Fo# in the lithospheric mantle because olivines in the present mantle xenoliths have Fo# of 88–92, which is within the range of a typical upper mantle. In addition, the P-wave velocity is not sensibly affected by water content in

the upper mantle, i.e., even if the upper mantle has a significant amount of water (ca. 10,000 ppm H/Si), the effect on the P-wave velocity is negligibly small (Karato, 1993, 1995). In fact, the mantle xenoliths show no trace of water such as hydrous minerals or hydrocarbon in fluid inclusions. Consequently, the low P-wave velocity anomaly is attributed mainly to higher temperature of the mantle.

Figure 4 depicts the temperature dependence of the P-wave velocity for peridotite. A difference in the P-wave velocity of 1% corresponds to that in 110°C for lherzolite. The geotherm for Archean cratons inferred from surface heat flow suggests mantle temperatures of around 400°C at 1 GPa (Currie and Hyndman, 2006). In contrast, the present mantle xenoliths show the equilibrium temperature of 912–1022°C and depth provenance of around 1 GPa. Comparing the P-wave velocity at 400°C with that of the equilibrium temperature, the lithospheric mantle, from where the mantle xenoliths were derived, has possibly had a negative P-wave velocity anomaly of 4.6–5.5%. Such a high anomaly cannot be explained merely by compositional difference, i.e., a compositional difference among lherzolite, harzburgite, and dunite engenders difference in P-wave anomaly of less than 2.5% at 400°C. Therefore, the P-wave velocity anomaly observed in

Far Eastern Russia is expected to reflect a high geothermal gradient.

The geotherm inferred from P–T information of the present mantle xenoliths projects a 5-million-year-old geotherm. The thermal structure with scale of several tens of kilometers is, however, undisturbed over 5 million years because the average distance of thermal diffusion in olivine is calculated as ca. 17 km in 5 million years at 1000°C (Gibert et al., 2005). One other point is the importance of applying the P–T information to geotherm estimation. For a thermally unsteady craton, the equilibrium temperature might not respond promptly to a rapid change in ambient temperature. In such a case, the P–T information of xenoliths is inappropriate as a representative of geotherm at the time of ascent of the xenoliths. For the present xenoliths, we worry less because a homogeneous distribution of major elements within minerals was shown by line analyses using EPMA, except for sample En2A. Apparently, a hot region exists beneath Far Eastern Russia.

### 6.3. Thin lithosphere in Far Eastern Russia

The possible occurrence of the hot region might engender a thin lithosphere. A thin lithosphere in this region is inferred from the xenolith geotherm. Given that a boundary between the lithosphere and the asthenosphere corresponds to the yield point of the mantle minerals, the lithosphere thickness can be estimated based on the rheological properties of the minerals, which depend on some factors such as temperature, pressure, differential stress, and the water content. We have observed neither hydrous minerals nor hydrous fluid inclusions in the mantle xenoliths. Therefore, the effect of water is not great for the lithospheric mantle in this region. The pressure effect on the strain rate of the mantle minerals is large only at high pressures of more than several gigapascals. For example, assuming a typical case of activation volume, the pressure change of 0.5 GPa at 1600 K engenders a change of strain rate by a factor of about two (Karato, 2008).

Consequently, the strength of the dry lithospheric mantle in a ductile regime is controlled preferentially by temperature. Generally, the lithospheric thickness is inferred as the intersection of the mantle geotherm with the 1300°C mantle adiabat (e.g., Artemieva, 2006; Kelly et al., 2003; Pollack et al., 1993). The xenolith geotherm estimated in this study intersects the mantle adiabat with a potential temperature of 1300°C at around 1.5

GPa (ca. 50 km in depth) (Fig. 3). Geophysical data indicate crustal thickness of 25–30 km in the eastern part of Far Eastern Russia (Karp and Lelikov, 1990). Therefore, the estimate for the lithospheric thickness presented above suggests that the lithospheric mantle in this region is thinner than the overlying crust. This is supporting evidence for the remarkably thin lithosphere and the occurrence of the hot region in this area.

Unfortunately we have no information about the evolution of lithospheric thickness in Far Eastern Russia. Based on a plate cooling model, it is reasonable to assume that the present region composed of Precambrian continental basement had had lithosphere as thick as a thermally steady craton. Consequently, the thin lithosphere deduced from P–T conditions of the xenoliths suggests the occurrence of lithospheric thinning in this area.

#### 6.4. Hot region beneath Far Eastern Russia

The occurrence of the hot region in the backarc was proposed originally by Miyashiro (1986) to explain the crustal ages of marginal basins in the western Pacific region by

gradual movement of a large-scale mantle upwelling. Apparently, two interpretations can be made of the origin of the hot region. One is mantle wedge convection associated with subduction resulting in the uniformly high backarc temperatures (e.g., Currie and Hyndman, 2006; Currie et al., 2004, 2008; Kukačka and Matyska, 2008). For this model, a weak lithosphere rheology is necessary (Currie et al., 2008; Kukačka and Matyska, 2008) to explain the observed surface heat flow in Cascade ( $75 \pm 15 \text{ mW/m}^2$ ), but it is not well supported by the rheological data. Furthermore, high heat flow of around  $100 \text{ mW/m}^2$  is expected in Far Eastern Russia, which is higher than that assumed in the mantle wedge convection model. High heat flow is also expected in northeastern China adjacent to Far Eastern Russia from anomalous P-wave velocity perturbation ( $< -6\%$ ) observed by local tomography of the lithospheric mantle (Huang and Zhao, 2009). Some alternative thermal process is necessary to explain the high heat flow in the backarc, especially for eastern Asia.

It is worth noting that the xenolith geotherm might not correspond to surface heat flow because it takes time for surface heat flow to reflect a thermal event in a mantle region. We briefly simulated the timescales of both thermal diffusion and reequilibration

of the geothermometer. As described in section 6.1, it takes 2.5 million years to reequilibrate a two-pyroxene thermometer at 1000°C. For mineral grains with ca. 2 mm diameter, ten million years are necessary to complete reequilibration. During the period, heat diffuses by about 30 km at 1000°C (Gibert et al., 2005). Although thermal diffusion is not so great in the continental crust, the timescale for the thermal conductance and the reequilibration has no appreciable difference. Consequently, thermal perturbation occurring in the uppermost mantle might appear on both surface heat flow and geothermometric data recorded in a mantle rock. Therefore, it would be necessary to compare the xenolith geotherm with the surface heat flow.

Another interpretation of the origin of the hot region inferred from the xenolith geotherm is asthenospheric upwelling associated with stagnant slab and subsequent lithospheric thinning. The asthenospheric upwelling associated with a stagnant slab and subsequent lithospheric thinning in eastern Asia are discussed based on both geochemical data of basaltic rocks and tectonic evidence (e.g., Nohda et al., 1988; Okamura et al., 2005; Tatsumi et al., 1990; Xu, 2001; Yang et al., 2003). Tatsumi and Eggins (1995) extended the asthenospheric upwelling model, namely a "harzburgite plume model" by

which a harzburgite body in the stagnant slab beneath the backarc region rises gravitationally and induces decompression melting of the body itself or thermal convection within the region, which engenders basalt volcanism in the backarc region with a distinct geochemical signature related to subduction. Actually, Okamura et al. (2005) reported that Cenozoic basalts in Far Eastern Russia show an EM-type signature in isotopic ratios of Sr, Nd, and Pb. Another extended asthenospheric upwelling model is the "wet region hypothesis" (Iwamori, 1992). The area beneath the backarc is under a wet condition derived from a fluid-rich deeper mantle, which causes a solidus temperature decrease.

Ichiki et al. (2006) tested the models using electrical conductivity and seismic P-wave velocity observation of the upper mantle beneath northeastern China. They obtained two model structures for the upper mantle. One supports the wet region hypothesis that the upper mantle above the stagnant slab comprises pyrolite with a moderate amount of water (500–1000 ppm H/Si). The other can support the harzburgite plume model by which the upper mantle is divided into two segments: hot and dry harzburgite shallower mantle and wet deeper mantle. The lithospheric properties inferred

from the present study are substantially compatible with the hot and dry shallower harzburgite mantle.

Zhao et al. (2004) proposed the Big Mantle Wedge (BMW) model to explain low P-wave velocity in the backarc mantle, in which the stagnant slab in the transition zone can play a necessary role in the intraplate volcanic activities above the stagnant slab. We explain the BMW model briefly according to a hypothesis related to magma generation in the BMW model (Maruyama et al., 2009; Ohtani and Zhao, 2009) as follows. Figure 5 depicts the BMW model modified slightly after the original one. Because of incomplete dehydration of the shallow subducting slab, hydrogen in hydrated peridotite at the bottom of the mantle wedge can be transported downward with corner flow in the mantle wedge (Iwamori, 2000). With increasing P–T values of the hydrated peridotite, partial melting occurs and produces hydrous magma in the deep upper mantle. Hydrous magma with H<sub>2</sub>O less than 5 wt% is gravitationally stable at a depth of around 410 km (Matsukage et al., 2005; Sakamaki et al., 2006; Suzuki et al., 1995). With increasing temperature of the transition zone above the stagnant slab, hydrogen solubility in transition zone minerals such as wadsleyite and ringwoodite decreases (Demouchy et al., 2005; Ohtani et al.,

2000). Then vertical advection of hydrogen released from the transition zone minerals enhances the water content of the magma. The successive increase of hydrogen content in the magma will eventually engender gravitational instability, resulting in ascent of the hydrous magma through a shallower part of the backarc upper mantle. Such magmatism might be responsible for warming of the backarc lithosphere, subsequent lithospheric thinning, and low P-wave velocity in the shallower part of the backarc upper mantle.

Assuming that the speculation presented above is an appropriate explanation for the cause of the hot region, the hot lithosphere should be distributed throughout eastern Asia. Cenozoic mantle xenoliths are visible in many places throughout eastern Asia. Arai et al. (2007) reviewed localities of mantle xenoliths in the western Pacific region and reported petrological data of representative samples. Furthermore, many studies have examined the mantle xenoliths, particularly addressing each locality: northeastern China (e.g., Choi et al., 2008; Tang et al., 2008), Mongolia (e.g., Ionov and Hofmann, 2007; Ionov et al., 2005a), Korea (Arai et al., 2001; Kim et al., 2005), Far Eastern Russia (e.g., Ionov et al., 2005b; Yamamoto et al., 2009), and Japan (e.g., Arai and Saeki, 1980; Takahashi, 1978 ). Accumulation of P–T information of the mantle xenoliths enables us to evaluate the

BMW model. In addition, considering eruption age of the mantle xenoliths, we can address lithospheric geotherm evolutional processes in eastern Asia: additional studies of an Asian xenolith geotherm are expected to reveal more about the spatial distribution of the hot region and its generation mechanism.

## 7. Conclusions

The depth provenance and the equilibrium temperature of the present mantle xenoliths are estimated respectively as 32–40 km and 912–1022°C. The P–T values correspond to heat flow of around 100 mW/m<sup>2</sup>, which reflects the high temperature of the backarc lithospheric mantle. For the Cascade, some studies have proposed numerical models to reproduce high surface heat flow of  $75 \pm 15$  mW/m<sup>2</sup> by mantle convection in the mantle wedge. However, it seems difficult to explain the high heat flow only by the mantle convection model because the xenolith geotherm in Far Eastern Russia is much higher than that assumed in the model.

Recent seismic tomography data clearly show a low P-wave velocity anomaly in the shallower part of the backarc upper mantle. To explain the P-wave velocity structure and intraplate magmatism in the backarc, the BMW model was proposed. The heat flow in Far Eastern Russia, which is comparable to that observed in the volcanic arc, is explainable using the BMW model. The combination of high-precision local seismic tomography and further studies of xenolith geotherm in backarc regions will help to evaluate the BMW model and to enhance understanding of mantle dynamics in the backarc.

## Acknowledgments

Two anonymous reviewers provided thoughtful comments that improved the manuscript. Comments on the elastic deformation model by Y. Zhang were helpful to correct the CO<sub>2</sub> density. Discussion with T. Ohkura and M. Ichiki related to the seismic wave velocity structure in the upper mantle was useful to improve the manuscript. We thank S. Goto for

comments related to heat flow in eastern Asia. This study was supported by a Grant-in-Aid of FGI and Grants-in-Aid for Scientific Research (No. 22109506) from the Japan Society for the Promotion of Science (JSPS).

## References

Ackerman, L., Mahlen, N., Jelínek, E., Medaris, G., Ulrych, J.Jr., Strnad, L., Mihaljevič, M., 2007. Geochemistry and evolution of subcontinental lithospheric mantle in central Europe: evidence from peridotite xenoliths of the Kozlov volcano, Czech Republic. *J. Petrol.* 48, 2235–2260.

Akinin, V.V., Foden, M.F., Francis, D., Apt, J., Moll-Stalcup, E., 1997. Compositional and thermal state of the upper mantle beneath the Bering Sea basalt province: evidence from the Chukchi Peninsula of Russia. *Can. J. Earth Sci.* 34, 789–800.

Andersen, T., Neumann, E.-R., 2001. Fluid inclusions in mantle xenoliths. *Lithos* 55, 301–320.

Arai, S., 1994. Characterization of spinel peridotites by olivine–spinel compositional relationships: Review and interpretation. *Chem. Geol.* 113, 191–204.

Arai, S., Saeki, Y., 1980. Ultramafic-mafic inclusions from Sannomegata crater, Oga Peninsula, Japan, with special reference to the Ichinomegata inclusions. *J. Geol. Soc. Japan* 86, 705–708.

Arai, S., Kida, M., Abe, N., Yurimoto, H., 2001. Petrology of peridotite xenoliths in alkali basalt (11 Ma) from Boun, Korea: an insight into the upper mantle beneath the East Asian continental margin. *J. Min. Pet. Sci.* 96, 89–99.

Arai, S., Abe, N., Ishimaru, S., 2007. Mantle peridotites from the Western Pacific. *Gondwana Res.* 11, 180–199.

Artemieva, I.M., 2006. Global  $1^\circ \times 1^\circ$  thermal model TC1 for the continental lithosphere: implications for lithosphere secular evolution. *Tectonophysics* 416, 245–277.

Bass, J.D., 1995. Elasticity of minerals, glasses and melts. *In*: T.J. Ahrens, Editor, Mineral Physics and Crystallography: A Handbook of Physical Constants, American Geophysical Union, Washington pp. 45–63.

Bence, A.E., Albee, A.L., 1968. Empirical correction factors for the electron microanalysis of silicates and oxides. *J. Geol.* 76, 382–403.

Blackwell, D.D., Steele, J.L., Frohme, M.K., Murphey, C.F., Priest, G.R., Black, G.L., 1990. Heat flow in the Oregon Cascade Range and its correlation with regional gravity, Curie point depths and geology. *J. Geophys. Res.* 95, 19475–19493.

Blackwell, D.D., Steele, J.L., Kelley, S., Korosec, M.A., 1990. Heat flow in the state of Washington and thermal conditions in the Cascade Range. *J. Geophys. Res.* 95, 19495–19516.

Choi, S.H., Mukasa, S.B., Zhou, X.-H., Xian, X.H., Andronikov, A.V., 2008. Mantle dynamics beneath East Asia constrained by Sr, Nd, Pb and Hf isotopic systematics of ultramafic xenoliths and their host basalts from Hannuoba, North China. *Chem. Geol.* 248, 40–61.

Currie, C.A., Wang, K., Hyndman, R.D., He, J., 2004. The thermal effects of steady-state slab-driven mantle flow above a subducting plate: the Cascadia subduction zone and backarc. *Earth Planet. Sci. Lett.* 223, 35–48.

Currie, C.A., Hyndman, R.D., 2006. The thermal structure of subduction zone back arcs. *J. Geophys. Res.* 111, B08404

Currie, C.A., Huisman, R.S., Beaumont, C., 2008. Thinning of the continental backarc lithosphere by flow-induced gravitational instability. *Earth Planet. Sci. Lett.* 269,

435–446.

Demouchy, S., Deloule, E., Frost, D.J., Keppler, H., 2005. Pressure and temperature-dependence of water solubility in Fe-free wadsleyite. *Am. Mineral.* 90, 1084–1091.

Doin, M.P., Fleitout, L., 1996. Thermal evolution of the oceanic lithosphere: an alternative view. *Earth Planet. Sci. Lett.* 142, 121–136.

Duan, Y., Zhao, D., Zhang, X., Xia, S., Liu, Z., Wang, F., Li, L., 2009. Seismic structure and origin of active intraplate volcanoes in Northeast Asia. *Tectonophysics* 470, 257–266.

Esin, S.V., Ponomarchuk, V.A., Shipitsin, Y.G., Palesskii, S.V., 1995. Petrogenesis of the Sovgavan tholeiite-alkaline basalt plateau in the eastern Sikhote-alin. *Russian Geology and Geophysics* 36, 60–68.

Gibert, B., Schilling, F.R., Gratz, K., Tommasi, A., 2005. Thermal diffusivity of olivine single crystals and a dunite at high temperature: evidence for heat transfer by radiation in the upper mantle. *Phys. Earth Planet. Int.* 151, 129–141.

Huang, J., Zhao, D., 2009. Seismic imaging of the crust and upper mantle under Beijing and surrounding regions. *Phys. Earth Planet. Int.* 173, 330–348.

Huang, Z., Zhao, D., Umino, N., Wang, L., Matsuzawa, T., Hasegawa, A., Yoshida, T., 2010. P-wave tomography, anisotropy and seismotectonics in the eastern margin of Japan Sea. *Tectonophysics* 489, 177–188.

Hyndman, R.D., Lewis, T.J., 1999. Geophysical consequences of the Cordillera-Craton thermal transition in southwestern Canada. *Tectonophysics* 306, 397–422.

Hyndman, R.D., Currie, C.A., Mazzoti, S., 2005. Subduction zone backarcs, continental mobile belts, and orogenic heat. *GSA Today* 15, 4–10.

Ichiki, M., Baba, K., Obayashi, M., Utada, H., 2006. Water content and geotherm in the upper mantle above the stagnant slab: Interpretation of electrical conductivity and seismic P-wave velocity models. *Phys. Earth Planet. Int.* 155, 1–15.

Ionov, D.A., Blichert-Toft, J., Weis, D., 2005a. Hf isotope compositions and HREE variations in off-craton garnet and spinel peridotite xenoliths from central Asia. *Geochim. Cosmochim. Acta* 69, 2399–2418.

Ionov, D.A., Prikhodko, V.S., Bodinier, J.-L., Sobolev, A.V., Weis, D., 2005b. Lithospheric mantle beneath the south-eastern Siberian craton: petrology of peridotite xenoliths in basalts from the Tokinsky Stanovik. *Contrib. Mineral. Petrol.* 149, 647–665.

Ionov, D.A., Hofmann, A.W., 2007. Depth of formation of subcontinental off-craton peridotites. *Earth Planet. Sci. Lett.* 261, 620–634.

Ishiwatari, A., Tsujimori, T., 2003. Paleozoic ophiolites and blueschists in Japan and Russian Primorye in the tectonic framework of East Asia: a synthesis. *The Island Arc* 12, 190–206.

Iwamori, H., 1992. Degree of melting and source composition of Cenozoic basalts in southwestern Japan: evidence for mantle upwelling by flux melting. *J. Geophys. Res.* 97, 10983–10995.

Iwamori, H., 2000. Deep subduction of H<sub>2</sub>O and deflection of volcanic chain towards backarc near triple junction due to lower temperature. *Earth Planet. Sci. Lett.* 181, 41–46.

Kaneoka, I., Notsu, K., Takigami, Y., Fujioka, K., Sakai, H., 1990. Constraints on the evolution of the Japan Sea based on <sup>40</sup>Ar–<sup>39</sup>Ar ages and Sr isotopic ratios for volcanic rocks of the Yamato Seamount chain in the Japan Sea. *Earth Planet. Sci. Lett.* 97, 211–225.

Karato, S.-I., 1993. Importance of anelasticity in the interpretation of seismic tomography. *Geophys. Res. Lett.* 20, 1623–1626.

Karato, S.-I., 1995. Effects of water on seismic wave velocities in the upper mantle. *Proc. Japan Acad.* 71, 61–66.

Karato, S., 2008. *Deformation of Earth Materials*. Cambridge University Press, New York, pp. 463.

Karp, B., Lelikov, E.P., 1990. Geological structure, composition and evolution of crustal layers of the Japan Sea. *Tectonophysics* 181, 277–283.

Kawakami, Y., Yamamoto, J., Kagi, H., 2003. Micro-Raman densimeter for CO<sub>2</sub> inclusions in mantle-derived minerals. *Appl. Spec.* 57, 1333–1339.

Kelly, R.K., Kelemen, P.B., Jull, M., 2003. Buoyancy of the continental upper mantle. *Geochem. Geophys. Geosys.* 4, 1017, doi:10.1029/2002GC000399.

Kim, K.H., Nagao, K., Tanaka, T., Sumino, H., Nakamura, T., Okuno, M., Lock, J.B., Youn, J.S., Song, J., 2005. He-Ar and Nd-Sr isotopic compositions of ultramafic xenoliths and host alkali basalts from the Korean peninsula. *Geochem. J.* 39, 341–356.

Kukačka, M., Matyska, C., 2008. Numerical model of heat flow in back-arc regions. *Earth Planet. Sci. Lett.* 276, 243–252.

Lucassen, F., Lewerenz, S., Franz, G., Viramonte, J., Mezger, K., 1999. Metamorphism, isotopic ages and composition of lower crustal granulite xenoliths from the Cretaceous Salta Rift, Argentina. *Contrib. Mineral. Petrol.* 134, 325–341.

Maruyama, S., Hasegawa, A., Santosh, M., Kogiso, T., Omori, S., Nakamura, H., Kawai, K., Zhao, D., 2009. The dynamics of big mantle wedge, magma factory, and metamorphic-metasomatic factory in subduction zones. *Gondwana Res.* 16, 414–430.

Matsukage, K.N., Jing, Z., Karato, S., 2005. Density of hydrous silicate melt at the condition of Earth's deep upper mantle. *Nature* 438, 488–491.

Milashev, V.A., 1988. Explosion Pipes. Springer-Verlag, New York, 249 pp.

Miller, C., Richter, W., 1982. Solid and fluid phases in lherzolite and pyroxenite inclusions from the Hoggar, central Sahara. *Geochem. J.* 16, 263–277.

Miyashiro, A., 1986. Hot regions and the origin of marginal basins in the western Pacific. *Tectonophysics* 122, 195–216.

Nohda, S., Tatsumi, Y., Otofuji, Y., Matsuda, T., Ishizaki, K., 1988. Asthenospheric injection and back-arc opening: isotopic evidence from Northeastern Japan. *Chem. Geol.* 68, 317–327.

Núñez-Valdez, M., Umemoto, K., Wentzcovitch, R.M., 2010. Fundamentals of elasticity of  $(\text{Mg}_{1-x},\text{Fe}_x)_2\text{SiO}_4$  olivine. *Geophys. Res. Lett.* 37, L14308, doi:10.1029/2010GL044205.

Ohtani, E., Zhao, D., 2009. The role of water in the deep upper mantle and transition zone: dehydration of stagnant slabs and its effects on the big mantle wedge. *Russian Geology and Geophysics* 50, 1073–1078.

Ohtani, E., Mizobata, H., Yurimoto, H., 2000. Stability of dense hydrous magnesium silicate phases in the systems  $\text{Mg}_2\text{SiO}_4\text{-H}_2\text{O}$  and  $\text{MgSiO}_3\text{-H}_2\text{O}$  at pressure up to 27 GPa. *Phys. Chem. Min.* 27, 533–544.

Okamura, S., Arculus, R.J., Martynov, Y.A., Kagami, H., Yoshida, T., Kawano, Y. 1998. Multiple magma sources involved in marginal-sea formation: Pb, Sr, and Nd isotopic evidence from the Japan Sea region. *Geology* 26, 619–622.

Okamura, S., Arculus, R.J., Martynov, Y.A., 2005. Cenozoic magmatism of the north-eastern Eurasian margin: the role of lithosphere versus asthenosphere. *J. Petrol.* 46, 221–253.

Pitzer, K.S., Sterner, S.M., 1994. Equations of state valid continuously from zero to extreme pressures for H<sub>2</sub>O and CO<sub>2</sub>. *J. Chem. Phys.*, 101, 3111–3116.

Pollack, H.N., Chapman, D.S., 1977. On the regional variation of heat flow, geotherms, and lithospheric thickness. *Tectonophysics* 38, 279–296.

Pollack, H.N., Hurter, S.J., Johnson, J.R., 1993. Heat flow from the Earth's interior: analysis of the global dataset. *Rev. Geophys.* 31, 267–280.

Roedder, E., 1983. Geobarometry of ultramafic xenoliths from Loihi Seamount, Hawaii, on the basis of CO<sub>2</sub> inclusions in olivine. *Earth Planet. Sci. Lett.* 66, 369–379.

Ross, J.V., 1983. The nature and rheology of the Cordilleran upper mantle of British Columbia: inferences from peridotite xenoliths. *Tectonophysics* 100, 321–357.

Sadeghi, H., Suzuki, S., Takenaka, H., 2000. Tomographic low-velocity anomalies in the uppermost mantle around the northeastern edge of Okinawa trough, the backarc of Kyushu. *Geophys. Res. Lett.* 27, 277–280.

Sakamaki, T., Suzuki, A., Ohtani, E., 2006. Stability of hydrous melt at the base of the Earth's upper mantle. *Nature* 439, 192–194.

Sapienza, G., Hilton, D.R., Scribano, V., 2005. Helium isotopes in peridotite mineral phases from Hyblean Plateau xenoliths (south-eastern Sicily, Italy). *Chem. Geol.* 219, 115–129.

Saruwatari, K., Ji, S., Long, C., Salisbury, M.H., 2001. Seismic anisotropy of mantle xenoliths and constraints on upper mantle structure beneath the southern Canadian Cordillera. *Tectonophysics* 339, 403–426.

Sato, K., 1999. Cenozoic volcanism in northern Sikhote Alin, Far East Russia and its implication for the opening of the Japan Sea. Ph.D. Thesis, Kyoto University, 126 pp.

Saxena, S.K., Chatterjee, N., Fei, Y., Shen, G., 1993. Thermodynamic data on oxides and silicates. Springer-Verlag, New York. 428 pp.

Schwab, R.G., Freisleben, B., 1988. Fluid CO<sub>2</sub> inclusions in olivine and pyroxene and their behaviour under high pressure and temperature conditions. *Bull. Mineral.* 111, 297–306.

Speziale, S., Jiang, F., Duffy, T.S., 2005. Compositional dependence of the elastic wave velocities of mantle minerals: implications for seismic properties of mantle rocks. *in* "Earth's Deep Mantle" (ed. R.D.v.d., Hilst, J.D., Bass, J., Matas, J., Trampert), pp. 301–320 American Geophysical Union.

Stein, C.A., Stein, S., 1992. A model for the global variation in oceanic depth and heat flow with lithospheric age. *Nature* 359, 123–129.

Suzuki, A., Ohtani, E., Kato, T., 1995. Flotation of diamond in mantle melt at high pressure. *Science* 269, 216–218.

Takahashi, E., 1978. Petrologic model of the crust and upper mantle of the Japanese island arcs. *Bull. Volcanol.* 41, 529–547.

Tang, Y.-J., Zhang, H.-F., Ying, J.-F., Zhang, J., Liu, X.-M., 2008. Refertilization of ancient lithospheric mantle beneath the central North China Craton: Evidence from petrology and geochemistry of peridotite xenoliths. *Lithos* 101, 435–452.

Tatsumi, Y., Eggins, S., 1995. Subduction Zone Magmatism. Blackwell Science, London 211pp.

Tatsumi, Y., Maruyama, S., Nohda, S., 1990. Mechanism of backarc opening in the Japan Sea: role of asthenospheric injection. *Tectonophysics* 181, 299–306.

Tatsumi, Y., Sato, K., Sano, T., Arai, R., Prikhodko, V.S., 2000. Transition from arc to intraplate magmatism associated with backarc rifting: evolution of the Sikhote Alin

volcanism. *Geophys. Res. Lett.* 27, 1587–1590.

Tian, Y., Zhao, D., Sun, R., Teng, J., 2009. Seismic imaging of the crust and upper mantle beneath the North China Craton. *Phys. Earth Planet. Int.* 172, 169–182.

Vacher, P., Mocquet, A., Sotin, C., 1996. Comparison between tomographic structures and models of convection in the upper mantle. *Geophys. J. Int.* 124, 45–56.

Weidner, D.J., Wang, H., Ito, J., 1978. Elasticity of orthoenstatite. *Phys. Earth Planet. Int.* 17, 7–13.

Wells, P.R.A., 1977. Pyroxene thermometry in simple and complex systems. *Contrib. Mineral. Petrol.* 62, 129–139.

Xu, Y.-G., 2001. Thermo-tectonic destruction of the archaean lithospheric keel beneath the Sino-Korean craton in China: evidence, timing and mechanism. *Phys. Chem. Earth (A)* 26, 747–757.

Yamamoto, J., Kagi, H., 2006. Extended micro-Raman densimeter for CO<sub>2</sub> applicable to mantle-originated fluid inclusions. *Chem. Lett.* 35, 610–611.

Yamamoto, J., Kagi, H., 2008. Application of micro-Raman densimeter for CO<sub>2</sub> fluid inclusions: a probe for elastic strengths of mantle minerals. *Eur. J. Mineral.* 20, 529–535.

Yamamoto, J., Kagi, H., Kaneoka, I., Lai, Y., Prikhod'ko, V.S., Arai, S., 2002. Fossil pressures of fluid inclusions in mantle xenoliths exhibiting rheology of mantle minerals: implications for the geobarometry of mantle minerals using micro-Raman spectroscopy. *Earth Planet. Sci. Lett.* 198, 511–519.

Yamamoto, J., Kaneoka, I., Nakai, S., Kagi, H., Prikhod'ko, V.S., Arai, S., 2004. Evidence for subduction-related components in the subcontinental mantle from low <sup>3</sup>He/<sup>4</sup>He and <sup>40</sup>Ar/<sup>36</sup>Ar ratio in mantle xenoliths from Far Eastern Russia. *Chem. Geol.* 207, 237–259.

Yamamoto, J., Kagi, H., Kawakami, Y., Hirano, N., Nakamura, M., 2007. Paleo-Moho depth determined from the pressure of CO<sub>2</sub> fluid inclusions: Raman spectroscopic barometry of mantle- and crust-derived rocks. *Earth Planet. Sci. Lett.* 253, 369–377.

Yamamoto, J., Ando, J., Kagi, H., Inoue, T., Yamada, A., Yamazaki, D., Irifune, T., 2008. In-situ strength measurements of natural upper-mantle minerals. *Phys. Chem. Minerals* 35, 249–257.

Yamamoto, J., Nakai, S., Nishimura, K., Kaneoka, I., Kagi, H., Sato, K., Okumura, T.,

Prikhod'ko, V.S., Arai, S., 2009. Intergranular trace elements in mantle xenoliths from Russian Far East: An example for mantle metasomatism by hydrous melt. *The Island Arc* 18, 225–241.

Yamamoto, J., Otsuka, K., Ohfuji, H., Ishibashi, H., Hirano, N., Kagi, H., 2011. Retentivity of CO<sub>2</sub> in fluid inclusions in mantle minerals. *Eur. J. Mineral.* 23, 805–815.

Yamano, M., Uyeda, S., 1988. Heat flow. *in* "The Ocean Basins and Margins, Vol. 7B, The Pacific Ocean", A.E.M., Nairn, F.G., Stehli, S., Uyeda, (eds.), 523–558, Plenum Publishing Corp., New York.

Yamano, M., 1995. Recent heat flow studies in and around Japan. *in* "Terrestrial Heat Flow and Geothermal Energy in Asia", edited by M.L., Gupta, M., Yamano, pp. 173–201, IBH, Bombay.

Yang, J.-H., Wu, F.-Y., Wilde, S.A., 2003. A review of the geodynamic setting of large-scale late Mesozoic gold mineralization in the north China craton: an association with lithospheric thinning. *Ore Geol. Rev.* 23, 125–152.

Zhang, Y., 1998. Mechanical and phase equilibria in inclusion–host systems. *Earth Planet. Sci. Lett.* 157, 209–222.

Zhang, X., Ganguly, J., Ito, M., 2010. Ca-Mg diffusion in diopside: tracer and chemical inter-diffusion coefficients. *Contrib. Mineral. Petrol.* 159, 175–186.

Zhao, D., Lei, J., Tang, R., 2004. Origin of the Changbai intraplate volcanism in Northeast China: evidence from seismic tomography. *Chinese Science Bulletin* 49, 1401–1408.

Zhao, D., Tian, Y., Lei, J., Liu, L., Zheng, S., 2009. Seismic image and origin of the Changbai intraplate volcano in East Asia: role of big mantle wedge above the stagnant Pacific slab. *Phys. Earth Planet. Int.* 173, 197–206.

Zhao, D., Pirajno, F., Dobretsov, N.L., Liu, L., 2010. Mantle structure and dynamics under East Russia and adjacent regions. *Russian Geology and Geophysics* 51, 925–938.

Zhao, D., Yu, S., Ohtani, E., 2011. East Asia: seismotectonics, magmatism and mantle dynamics. *J. Asia. Earth Sci.* 40, 689–709.

Zonenshain, L.P., Kuzmin, M.I., Natapov, L.M., 1990. Geology of the USSR: a Plate-Tectonic Synthesis. *American Geophysical Union, Geodynamic Series* 21, 242.

**Table 1. Average core compositions (wt%) of minerals in ultramafic xenoliths from Ennokentiev, Far Eastern Russia.**

| sample                         | En-1              |        |        |        | En21              |        |        |        | En-44             |        |        |        |
|--------------------------------|-------------------|--------|--------|--------|-------------------|--------|--------|--------|-------------------|--------|--------|--------|
| rock type                      | Spinel-lherzolite |        |        |        | Spinel-lherzolite |        |        |        | Spinel-lherzolite |        |        |        |
| mineral                        | olivine           | opx    | cpx    | spinel | olivine           | opx    | cpx    | spinel | olivine           | opx    | cpx    | spinel |
| Mg#                            | 88.42             | 88.84  | 89.28  | 73.38  | 90.27             | 91.40  | 90.40  | 82.21  | 88.18             | 88.25  | 87.80  | 73.11  |
| Cr#                            |                   |        |        | 12.25  |                   |        |        | 11.44  |                   |        |        | 8.90   |
| SiO <sub>2</sub>               | 39.86             | 54.37  | 51.78  | 0.05   | 40.07             | 54.72  | 52.26  | 0.05   | 40.22             | 54.34  | 52.55  | 0.07   |
| TiO <sub>2</sub>               | 0.02              | 0.11   | 0.51   | 0.20   | 0.01              | 0.12   | 0.48   | 0.14   | 0.00              | 0.12   | 0.50   | 0.17   |
| Al <sub>2</sub> O <sub>3</sub> | 0.19              | 4.57   | 6.77   | 55.54  | 0.02              | 4.79   | 6.77   | 56.35  | 0.02              | 5.18   | 7.41   | 57.30  |
| Cr <sub>2</sub> O <sub>3</sub> | 0.00              | 0.31   | 0.73   | 11.56  | 0.02              | 0.41   | 0.84   | 10.86  | 0.01              | 0.34   | 0.70   | 8.35   |
| FeO                            | 11.22             | 7.23   | 3.16   | 12.64  | 9.55              | 5.57   | 2.92   | 10.87  | 11.40             | 7.43   | 3.63   | 13.31  |
| MnO                            | 0.14              | 0.13   | 0.08   | 0.01   | 0.14              | 0.15   | 0.09   | 0.13   | 0.15              | 0.15   | 0.10   | 0.11   |
| MgO                            | 48.10             | 32.30  | 14.75  | 19.55  | 49.72             | 33.25  | 15.42  | 21.21  | 47.72             | 31.32  | 14.63  | 20.30  |
| CaO                            | 0.06              | 0.71   | 20.17  | 0.00   | 0.06              | 0.77   | 19.67  | 0.00   | 0.06              | 0.81   | 18.08  | 0.00   |
| Na <sub>2</sub> O              | 0.01              | 0.15   | 1.86   | 0.00   | 0.01              | 0.12   | 1.51   | 0.00   | 0.01              | 0.20   | 2.24   | 0.00   |
| K <sub>2</sub> O               | 0.01              | 0.01   | 0.01   | 0.01   | 0.00              | 0.00   | 0.01   | 0.01   | 0.00              | 0.00   | 0.00   | 0.00   |
| NiO                            | 0.38              | 0.10   | 0.04   | 0.39   | 0.39              | 0.10   | 0.04   | 0.39   | 0.34              | 0.09   | 0.04   | 0.38   |
| P <sub>2</sub> O <sub>5</sub>  | 0.00              | 0.00   | 0.10   | 0.00   | 0.00              | 0.00   | 0.00   | 0.00   | 0.05              | 0.02   | 0.12   | 0.01   |
| V <sub>2</sub> O <sub>3</sub>  | 0.01              | 0.01   | 0.04   | 0.05   | 0.00              | 0.00   | 0.00   | 0.00   | 0.00              | 0.00   | 0.00   | 0.00   |
| Total                          | 100.00            | 100.00 | 100.00 | 100.00 | 100.00            | 100.00 | 100.00 | 100.00 | 100.00            | 100.00 | 100.00 | 100.00 |
| T (°C)                         |                   |        |        | 912    |                   |        |        | 1022   |                   |        |        | 1013   |

(opx: orthopyroxene, cpx: clinopyroxene). Equilibrium temperatures (T) were estimated using the two-pyroxene geothermometer described in Wells (1977).

**Table 1. continued.**

| sample<br>rock type<br>mineral | En2A              |        |        |        | En-010            |        |        |        | En-41             |        |        |        |
|--------------------------------|-------------------|--------|--------|--------|-------------------|--------|--------|--------|-------------------|--------|--------|--------|
|                                | Spinel-Iherzolite |        |        |        | Spinel-Iherzolite |        |        |        | Spinel-Iherzolite |        |        |        |
|                                | olivine           | opx    | cpx    | spinel | olivine           | opx    | cpx    | spinel | olivine           | opx    | cpx    | spinel |
| Mg#                            | 92.28             | 90.07  | 90.59  | 80.93  | 89.57             | 90.19  | 90.64  | 74.85  | 90.07             | 90.41  | 91.35  | 77.87  |
| Cr#                            |                   |        |        | 12.89  |                   |        |        | 12.08  |                   |        |        | 9.60   |
| SiO <sub>2</sub>               | 39.76             | 54.79  | 52.23  | 0.04   | 40.07             | 54.61  | 51.83  | 0.04   | 40.44             | 54.86  | 52.44  | 0.01   |
| TiO <sub>2</sub>               | 0.01              | 0.10   | 0.42   | 0.10   | 0.01              | 0.12   | 0.53   | 0.17   | 0.00              | 0.12   | 0.51   | 0.03   |
| Al <sub>2</sub> O <sub>3</sub> | 0.02              | 4.35   | 5.67   | 54.75  | 0.02              | 4.60   | 6.81   | 55.83  | 0.00              | 4.55   | 6.94   | 58.62  |
| Cr <sub>2</sub> O <sub>3</sub> | 0.02              | 0.40   | 1.10   | 12.07  | 0.01              | 0.26   | 0.65   | 11.44  | 0.00              | 0.35   | 0.79   | 9.28   |
| FeO                            | 11.26             | 6.44   | 3.02   | 11.84  | 10.20             | 6.39   | 2.78   | 12.00  | 9.70              | 6.23   | 2.46   | 10.61  |
| MnO                            | 0.16              | 0.15   | 0.10   | 0.14   | 0.12              | 0.13   | 0.07   | 0.03   | 0.15              | 0.15   | 0.09   | 0.11   |
| MgO                            | 48.31             | 32.78  | 15.90  | 20.69  | 49.10             | 32.95  | 15.13  | 20.03  | 49.33             | 32.95  | 14.55  | 20.95  |
| CaO                            | 0.06              | 0.68   | 20.00  | 0.00   | 0.05              | 0.69   | 20.25  | 0.01   | 0.01              | 0.62   | 20.19  | 0.00   |
| Na <sub>2</sub> O              | 0.01              | 0.18   | 1.48   | 0.01   | 0.01              | 0.13   | 1.77   | 0.01   | 0.00              | 0.09   | 1.93   | 0.00   |
| K <sub>2</sub> O               | 0.00              | 0.00   | 0.03   | 0.00   | 0.01              | 0.01   | 0.01   | 0.01   | 0.00              | 0.00   | 0.00   | 0.00   |
| NiO                            | 0.37              | 0.10   | 0.05   | 0.37   | 0.40              | 0.10   | 0.05   | 0.38   | 0.35              | 0.08   | 0.03   | 0.36   |
| P <sub>2</sub> O <sub>5</sub>  | 0.00              | 0.00   | 0.00   | 0.00   | 0.00              | 0.00   | 0.09   | 0.01   | 0.02              | 0.01   | 0.06   | 0.02   |
| V <sub>2</sub> O <sub>5</sub>  | 0.00              | 0.00   | 0.00   | 0.00   | 0.01              | 0.02   | 0.03   | 0.05   | 0.00              | 0.00   | 0.00   | 0.00   |
| Total                          | 100.00            | 100.00 | 100.00 | 100.00 | 100.00            | 100.00 | 100.00 | 100.00 | 100.00            | 100.00 | 100.00 | 100.00 |
| T (°C)                         |                   |        |        | 980*   |                   |        |        | 931    |                   |        |        | 913    |

(opx: orthopyroxene, cpx: clinopyroxene). Equilibrium temperatures (T) were estimated using the two-pyroxene geothermometer described in Wells (1977). Data of En-010 is from Yamamoto and Kagi (2008). \*This value was obtained using averaged CaO content of cpx, which showed two peaks in CaO contents of 19.7wt% and 21.5wt%.

**Table 2. Results of micro-Raman spectroscopic analyses.**

|        | olivine<br>Delta (cm <sup>-1</sup> ) | orthopyroxene<br>Delta (cm <sup>-1</sup> ) | clinopyroxene<br>Delta (cm <sup>-1</sup> ) | spinel<br>Delta (cm <sup>-1</sup> ) |
|--------|--------------------------------------|--------------------------------------------|--------------------------------------------|-------------------------------------|
| En-1   | 104.989 ± 0.089                      | 105.529 ± 0.101                            | 105.525 ± 0.073                            | 105.740 ± 0.030                     |
| En2I   | 104.830 ± 0.084                      | 105.539 ± 0.084                            |                                            |                                     |
| En-44  |                                      | 105.576 ± 0.011                            | 105.659 ± 0.046                            |                                     |
| En2A   | 104.829 ± 0.077                      | 105.439 ± 0.059                            | 105.456 ± 0.030                            |                                     |
| En-010 | 105.182 ± 0.160                      | 105.532 ± 0.023                            | 105.564 ± 0.013                            | 105.781 ± 0.038                     |

Data of En-010 include those reported in Yamamoto and Kagi (2008). Delta value is separation of wavenumber between two main peaks of Raman spectra of CO<sub>2</sub>.

**Table 3. CO<sub>2</sub> density of CO<sub>2</sub> inclusions.**

|                      |             | En-1    |       |       |         | En21    |       | En-44  |       |
|----------------------|-------------|---------|-------|-------|---------|---------|-------|--------|-------|
|                      |             | olivine | opx   | cpx   | spinel  | olivine | opx   | opx    | cpx   |
| Density              | median      | 1.013   | 1.147 | 1.146 | 1.182   | 0.964   | 1.149 | 1.156  | 1.170 |
| (g/cm <sup>3</sup> ) | upper value | 1.039   | 1.165 | 1.159 | 1.187   | 0.990   | 1.164 | 1.158  | 1.177 |
|                      | lower value | 0.986   | 1.127 | 1.132 | 1.178   | 0.936   | 1.132 | 1.154  | 1.162 |
|                      |             | En2A    |       |       | En-010  |         |       |        |       |
|                      |             | olivine | opx   | cpx   | olivine | opx     | cpx   | spinel |       |
| Density              | median      | 0.963   | 1.129 | 1.132 | 1.067   | 1.148   | 1.153 | 1.189  |       |
| (g/cm <sup>3</sup> ) | upper value | 0.988   | 1.141 | 1.138 | 1.107   | 1.152   | 1.156 | 1.194  |       |
|                      | lower value | 0.938   | 1.116 | 1.126 | 1.023   | 1.143   | 1.151 | 1.183  |       |

(opx: orthopyroxene, cpx: clinopyroxene). CO<sub>2</sub> density were calculated using a relationship between Delta value and CO<sub>2</sub> density (Yamamoto and Kagi, 2006).

**Table 4. Corrected CO<sub>2</sub> density and depth provenance of the mantle xenoliths.**

|                                                                                             | En-1        | En2I   | En-44  | En2A   | En-010 |       |
|---------------------------------------------------------------------------------------------|-------------|--------|--------|--------|--------|-------|
| $\Delta V/V_0$ (%)                                                                          | -0.936      | -1.093 | -1.058 | -1.089 | -0.962 |       |
| CO <sub>2</sub> density (g/cm <sup>3</sup> )<br>of opx corrected for<br>elastic deformation | median      | 1.136  | 1.136  | 1.143  | 1.117  | 1.137 |
|                                                                                             | upper value | 1.154  | 1.151  | 1.145  | 1.128  | 1.141 |
|                                                                                             | lower value | 1.116  | 1.120  | 1.142  | 1.104  | 1.132 |
| Equilibrium temperature (°C)                                                                | 912         | 1022   | 1013   | 980    | 931    |       |
| P (GPa)                                                                                     | median      | 0.962  | 1.048  | 1.060  | 0.967  | 0.977 |
|                                                                                             | upper value | 1.036  | 1.115  | 1.091  | 1.020  | 1.015 |
|                                                                                             | lower value | 0.887  | 0.981  | 1.030  | 0.911  | 0.943 |
| Depth (km)                                                                                  | median      | 34.8   | 37.9   | 38.3   | 34.9   | 35.3  |
|                                                                                             | upper value | 37.4   | 40.3   | 39.4   | 36.8   | 36.7  |
|                                                                                             | lower value | 32.0   | 35.5   | 37.2   | 32.9   | 34.1  |

Elastic change in CO<sub>2</sub> density was corrected by following the correction method proposed by Zhang (1998).

## Figure captions

**Figure 1.** Map of eastern Asia. Mantle xenoliths were sampled from Ennokentiev, Far Eastern Russia, which is marked by a star. Gray and a black dotted lines show the inferred extents of the stagnant slab and P-wave velocity at a depth of 100 km with 1% slower than ambient mantle region indicated by a circle. A solid line is a profile of a schematic cross section of Fig. 5. A shaded area colored in dark gray depicts the area of extension of the Sea of Japan. DPRK and ROK respectively denote the Democratic People's Republic of Korea and the Republic of Korea.

**Figure 2.** Photograph of a thick section of a mantle xenolith (En2A). CO<sub>2</sub> inclusions in olivine show a negative crystal shape.

**Figure 3.** P–T diagram for the system CO<sub>2</sub> from Pitzer and Sterner (1994). Grey contours represent density in g/cm<sup>3</sup> (i.e. isochors). The pressure at which the mantle xenoliths were trapped by host magma can be estimated from intersections of the isochors with

equilibrium temperatures. Stars show the intersections. Uncertainties of the P–T values are within the size of symbols. Black solid lines show modeled geotherms. Numbers labeling the lines denote the corresponding heat flows in units of  $\text{mW/m}^2$ , which are referred from Pollack and Chapman (1977). The P–T values of the mantle xenoliths are consistent with heat flow of around  $100 \text{ mW/m}^2$  or higher.

**Figure 4.** Temperature dependence of the P-wave velocity. The P-wave velocity is calculated using following the calculation method of Vacher et al. (1998), which incorporates the elastic properties of the mantle. We assume modal mineral proportions of the media as follows. The lherzolite contains 69 vol% olivine, 20 vol% orthopyroxene, 10 vol% clinopyroxene and 1 vol% spinel. The harzburgite contains 89 vol% olivine, 10 vol% orthopyroxene and 1 vol% spinel. The dunite contains 99 vol% olivine and 1 vol% spinel. Elastic constants for the minerals are from Bass (1995). It is to be noted that the anelastic effect of mantle minerals can be significant at  $> \text{ca. } 900^\circ\text{C}$  (Karato, 1993). Consequently, the temperature dependence in the temperatures of  $> \text{ca. } 900^\circ\text{C}$  is the lower limit.

**Figure 5.** Schematic cross-section beneath eastern Asia. The explanation is presented in the text. The horizontal to vertical ratio is approximately 1. The relation between the backarc magmatism and host magma of the present xenoliths remains unclear.

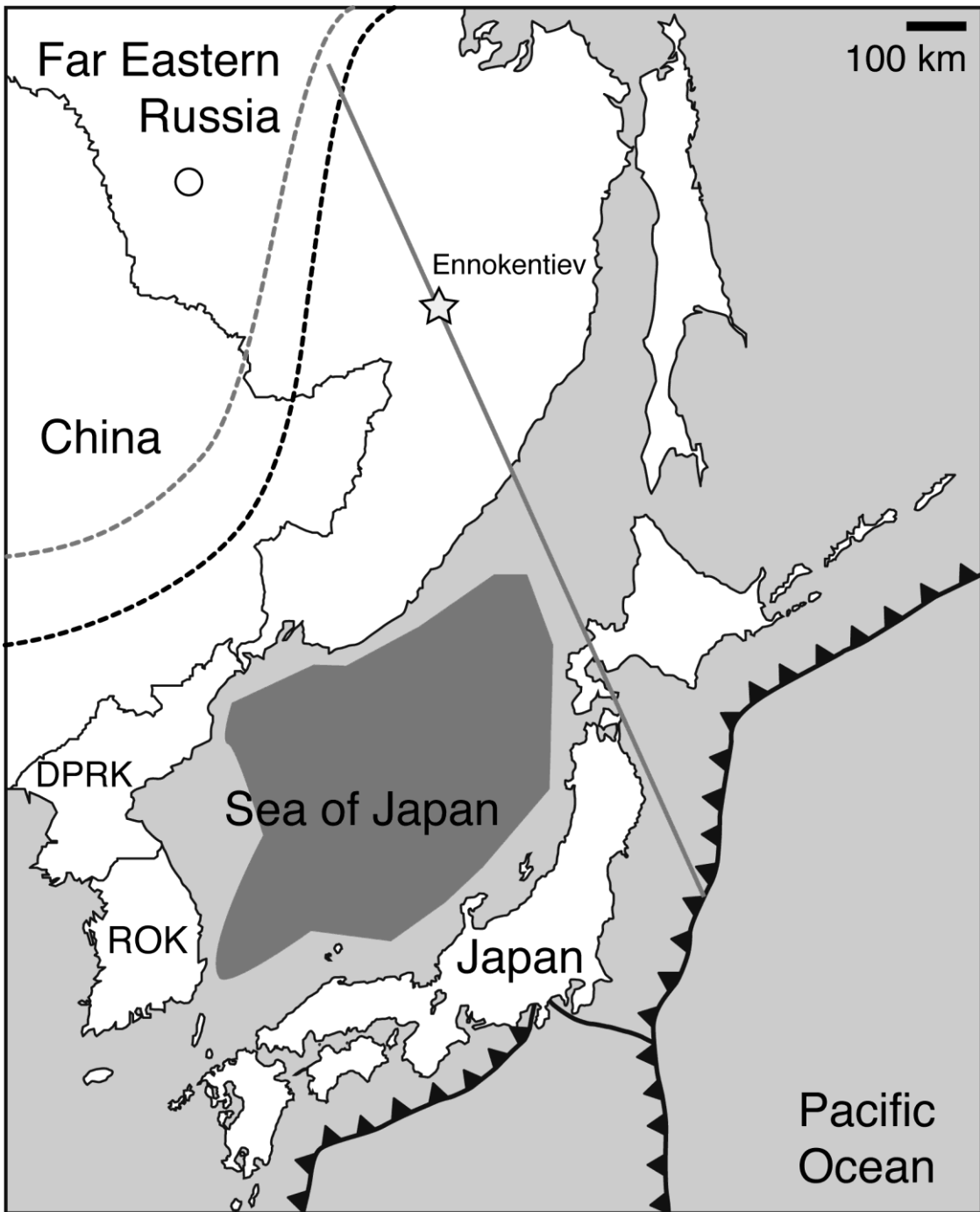


**Fig. 1**

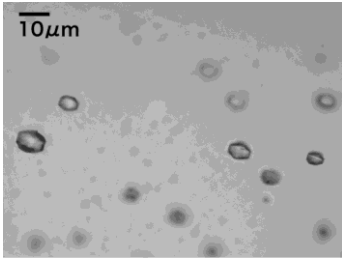


**Fig. 2**

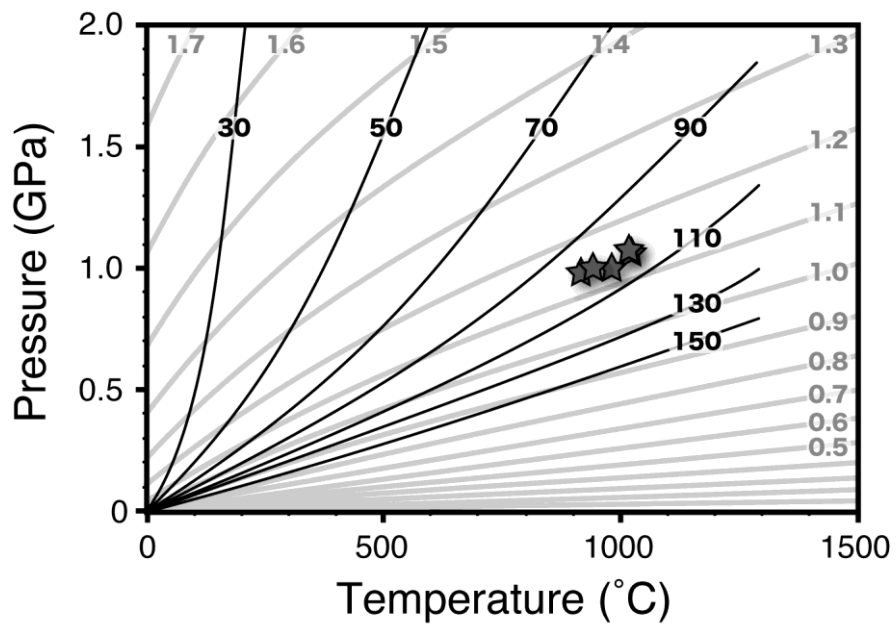


**Fig. 3**

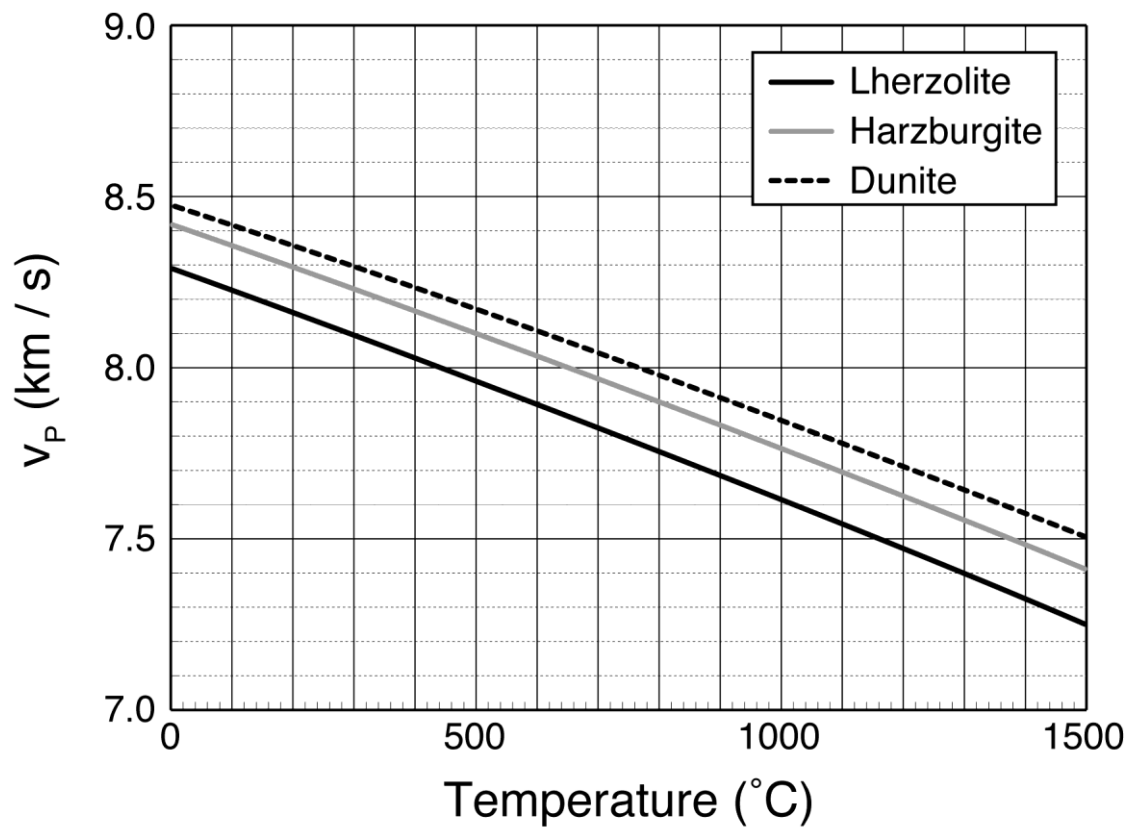


**Fig. 4**

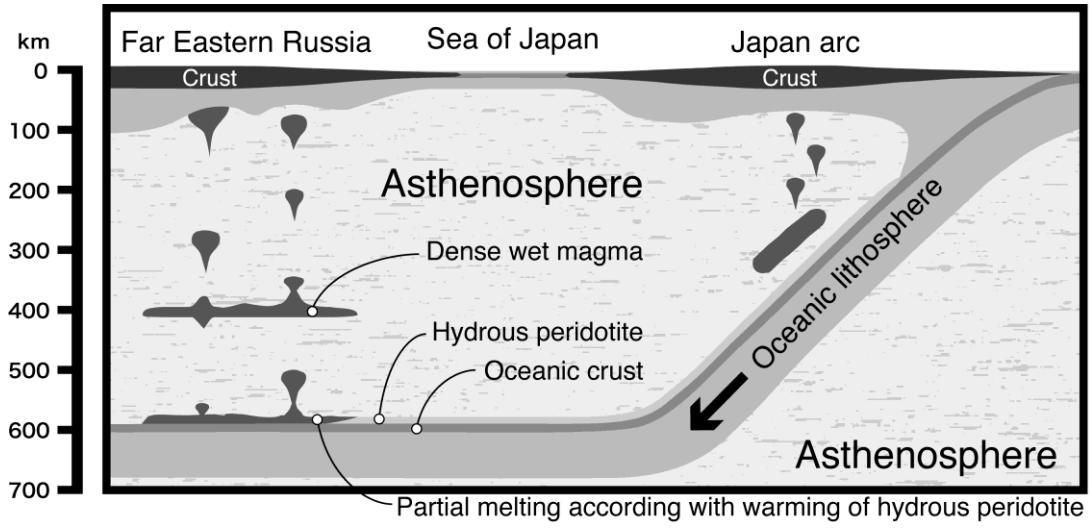


**Fig. 5**